*J. Plasma Physics* (1987), *vol.* 37, *part* 2, *pp.* 185–198
*Printed in Great Britain*



# The interaction of a conducting object with a supersonic plasma flow: ion deflection near a negatively charged obstacle

By R. L. MERLINO AND N. D'ANGELO
Department of Physics & Astronomy, The University of Iowa,
Iowa City, Iowa 52242-1410

(Received 20 June 1986 and in revised form 15 August 1986)

An experimental study of the interaction of a conducting object with a flowing plasma is described. Particular attention is given to the deflection of ions in the sheath of a negatively charged body. The experiments were conducted in a double plasma device in which a relatively weak longitudinal magnetic field may also be present. For the particular conditions used in these experiments, it was found that ion deflection occurs primarily near the edge of the body. A simple physical model is discussed which accounts for the observed dependences of the convergence of ion streams on the body potential and ion beam velocity. A density rarefaction wave is also observed in the wake region, which propagates into the ambient plasma at roughly the ion acoustic Mach angle. Finally, some preliminary observations of the spatial distribution of plasma noise in the wake region are presented.

## 1. Introduction

In this paper we report results of a laboratory study of the disturbance produced by a conducting body downstream of a plasma flow. This problem, which is relevant to the assessment of the spacecraft–environment interaction, has continued to receive considerable attention (Nosachev & Skvortsov 1978; Murphy *et al.* 1986; Wright, Stone & Samir 1985; Stone 1981*a*, *b*; Raychaudhuri *et al.* 1986; Samir, Wright & Stone 1983). In the frame of reference of a spacecraft moving through the ionosphere at several km $s^{-1}$, a supersonic plasma flow is present with a flow speed, $v$, characterized by $C_s \ll v \ll v_{e,\mathrm{th}}$, where $C_s$ is the ion acoustic speed and $v_{e,\mathrm{th}}$ is the electron thermal speed; this situation is also present in most laboratory plasma wake experiments. The theoretical and experimental studies have centred upon three main aspects of the body–flow interaction: (i) the structure of the ion-void region in the wake of the body, (ii) the expansion of plasma into the wake and the ion density rarefaction at the wake edge, and (iii) the axial ion enhancement present some distance downstream of negatively charged bodies. Our present study has concentrated mainly on point (iii), and is relevant to any situation involving the flow of plasma near an electrically floating object which will be negatively charged as a result of the higher mobility of electrons compared with that of the ions.

The axial ion enhancement just downstream of a body in a plasma flow has been observed previously (Stone, Oran & Samir 1972; Stone 1981*a*, *b*) and has

usually been attributed to electrostatic focusing of ion streams onto the wake axis (Martin 1974; Taylor 1967). A detailed review is given in the thesis of Stone (1979). The electric fields are associated with (*a*) the sheath near the negatively charged body and/or (*b*) the potential gradients set up at the wake edge. The latter are present since electrons can move into the wake (in the absence of a magnetic field) faster than the ions. If both effects (*a*) and (*b*) occur, the resultant electric field may extend from the body into the wake along the wake edge, giving rise to a deflection of the ions onto the wake axis (Taylor 1967). The converging ion streams originating all around the body edge are usually characterized by the downstream distance from the body to the location of the convergence point where the ion density is largest. This position depends upon the body potential and ion flow speed (Mach number); the actual relationship being detemined by which of the two mechanisms, (*a*) or (*b*) discussed above, is more important.

In our work, which was carried out in a double plasma device, we studied the effects of varying the body potential $V_b$ and Mach number $M$ on the converging ion streams. Our experiments were carried out in the parameter range where the appropriate dimensionless parameters which characterize the flow–body interaction have the following values: $R/\lambda_D \approx 5$–$20$, $eV_b/kT_e \approx 2$–$20$, and $M = V_0/C_s \approx 2$–$4$, where $R$ is the body radius, $\lambda_D$ the Debye length, $V_0$ the plasma flow velocity, and $C_s$ is the ion acoustic speed.

By using a segmented body (disk+ring) we were able to show that the deflection of ions into the wake is connected with the presence of a negative potential near the edge of the body. We also had the possibility of applying a weak magnetic field (sufficient to magnetize the electrons but not the ions) aligned along the plasma flow. The effect of this magnetic field on the potential in the wake has already been reported (D'Angelo & Merlino 1986). Finally, we will present some preliminary results on the spatial structure of plasma turbulence in the wake region.

This paper is organized as follows. In §2 we describe the experimental method and the diagnostics. The experimental results are presented in §3 and a discussion of these results follows in §4.

## 2. Experimental method

Our experiments were carried out in the double-plasma (DP) device shown schematically in figure 1. An external set of coils allows application of an axial magnetic field up to about 100 G in the centre of the device. The plasma is produced by a discharge in argon gas in the 'driver' chamber (discharge voltage $= -50$ V). The 'driver' and 'target' chambers are separated by a grid biased at $-62$ V to prevent primary electrons from entering the target. When the 'cage' is biased positive, an ion beam (of variable energy depending on the cage bias) is injected into the target. The target filaments provide electrons to neutralize the ion charge, but these electrons do not produce a discharge in the target since the target filaments are usually biased only to $-15$ V relative to the walls. This mode of operation of the DP device allows us to have a flowing plasma in the target chamber, with a density that can be much larger than the density of the background (thermal) plasma. At the typical operating (argon) pressure of $\approx 3 \times 10^{-5}$ torr, the density of the flowing plasma is $\approx 10^8$–$10^9$ cm$^{-3}$.

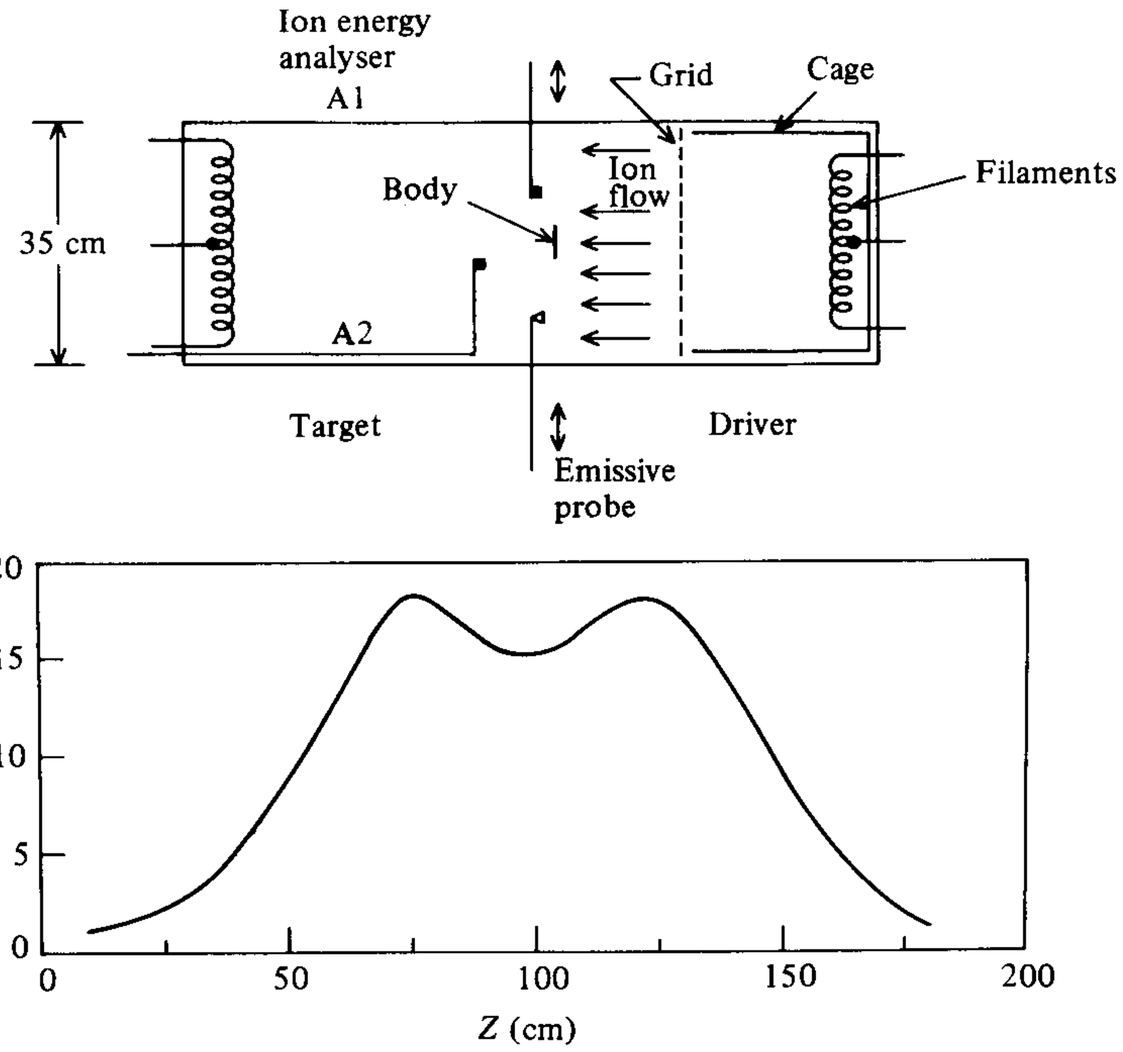


FIGURE 1. Schematic of the experimental set-up. The profile of the axial magnetic field (produced by coils not shown), for a coil current of 10 A, is also shown on the same scale.

The density of the background plasma is, typically, a factor of 2–5 lower. This low pressure ensures that plasma production by charge exchange in the target is minimal, since the $A^+ - A$ charge exchange mean free path is $\approx 2$ metres ($\sigma_{A-A^+} \approx 5 \times 10^{-15}$ cm$^2$); however, the background target plasma density is still provided by the infrequent charge exchange collisions.

The 'body' (or obstacle) used in our studies was a 3 cm diameter, 0·8 mm thick tantalum disk located on the axis of the device and oriented normal to the ion flow. The disk could be electrically floated or biased to any desired potential. For one series of experiments we used a split 'body' consisting of coplanar ring (3 cm OD, 2·4 cm ID) and inner disk (2·2 cm diameter) separated by a ceramic insulator and both 0·8 mm thick. The disk and ring could be biased separately.

Measurements of the ion beam flux and thermal background plasma flux were performed using two gridded ion-energy analysers. One analyser (A1) could be moved radially at a fixed distance of about 4·5 cm behind the obstacle, while the other (identical) one (A2) could be moved both radially and axially to map out the full wake structure. The analysers had an overall diameter of 1 cm and used two grids each consisting of 40 lines per cm tungsten mesh. The outer grid was kept at ground potential, the retarding voltage was applied to the second grid, and the collector was biased at $-90$ V. The retarding grid could be either swept in voltage to produce a full characteristic analyser curve or, by applying a sufficiently large positive bias on it, could be used to measure the flux of beam ions at a fixed energy. In the latter mode, the analyser acts essentially as a Faraday cup. The angular acceptance of the analyser was rather large so that ion velocity vector measurements could not be made. In addition to the ion flux

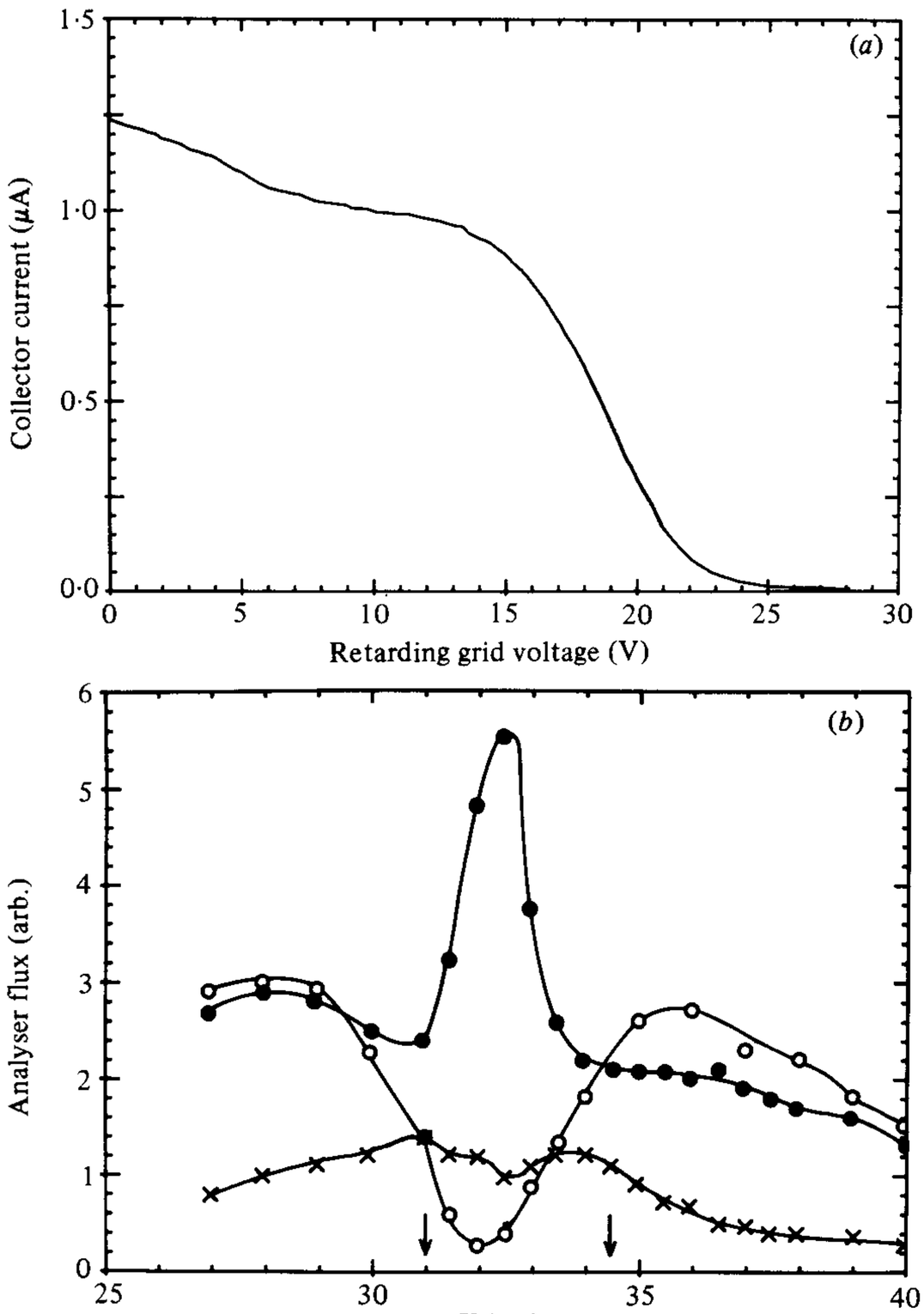


FIGURE 2. Ion energy analyser measurements of beam and thermal fluxes. (*a*) A typical collector current *vs.* retarding voltage characteristic. (*b*) Radial profiles of beam and thermal flux at 4·5 cm downstream of the obstacle. The edges of the obstacle are indicated by vertical arrows. ○, beam flux (body grounded); ●, beam flux (body floating); ×, thermal flux.

measurements in the wake, potential measurements were made using an emissive probe that could only be moved radially at a fixed position (4·5 cm) behind the body. The results of these potential measurements are given in a separate report (D'Angelo & Merlino 1986).

## 3. Experimental results

In this section we present the experimental results on (*a*) the spatial profiles of ion fluxes in the wake (ion focusing) and (*b*) plasma noise in the wake.

### 3.1. *Ion focusing into the wake*

We describe here the results of measurements of ion flux made with the ion energy analysers behind the body. The first set of measurements refer to the

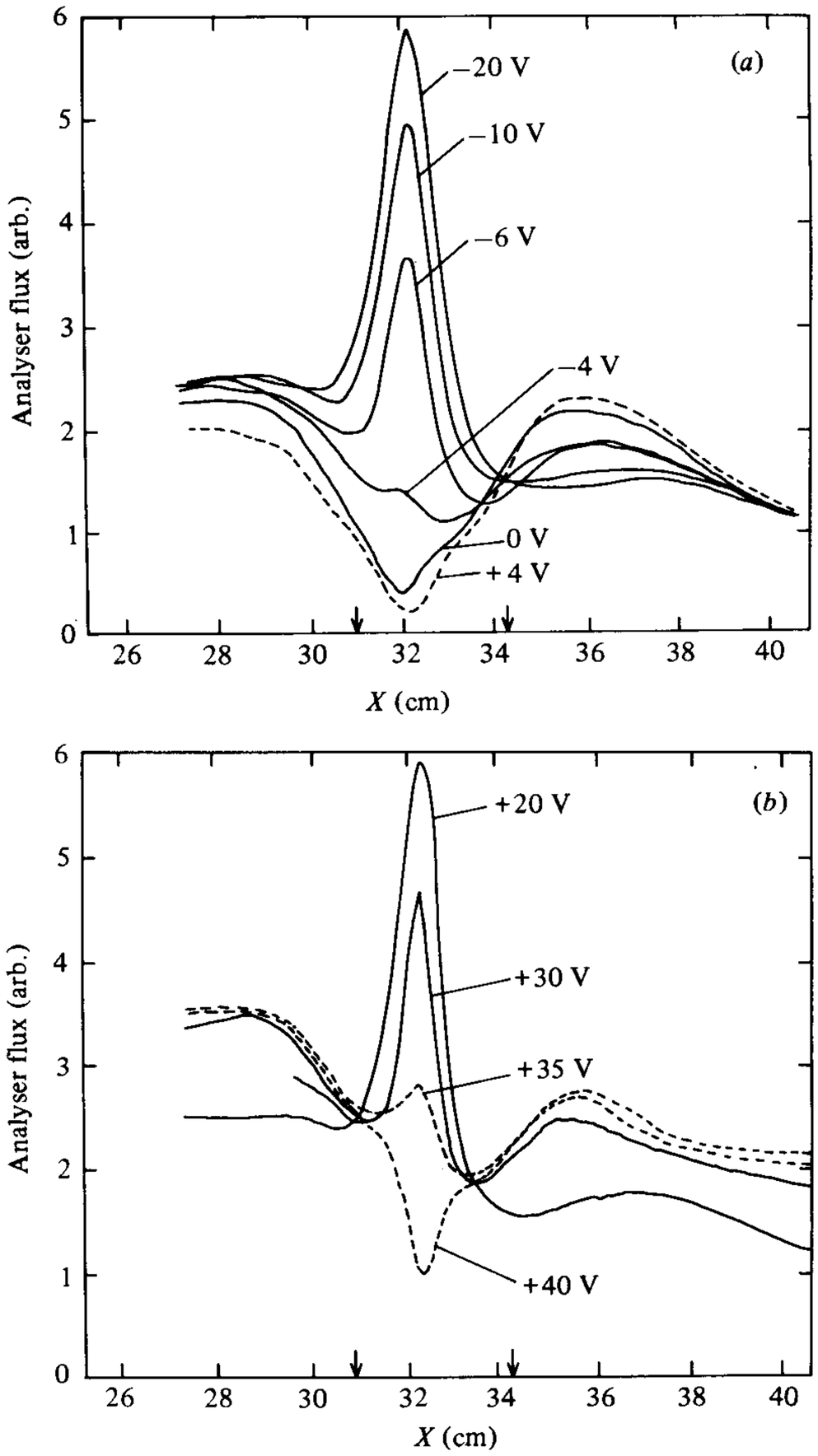


FIGURE 3. Analyser beam flux profiles at 4·5 cm downstream of the obstacle. (*a*) Beam flux profiles at fixed cage voltage (13 V) and various body potentials (shown against the curves). (*b*) Beam flux profiles at fixed body potential (−10 V) and varying cage voltage (shown against the curves). Note that the ordinate scales in (*a*) and (*b*) are not the same. $P = 5 \times 10^{-5}$ torr, $B_0 = 8$ G.

3 cm diameter disk. Using analyser A1, we took a series of traces of collector current *vs.* retarding voltage at various positions across the ion flow, and for a number of different disk bias voltages. These data were taken under the conditions: $p = 5 \times 10^{-5}$ torr (argon), $B_0 = 8$ G, and $V_{\text{cage}} = 13$ V (ion beam energy $\approx 17$ eV). From the full analyser characteristics, a typical example of which is shown in figure 2(*a*), we construct profiles of ion beam flux and thermal background ion flux. Two such profiles, taken with the body floating and grounded are shown in figure 2(*b*). For this set of data, the filament bias in the

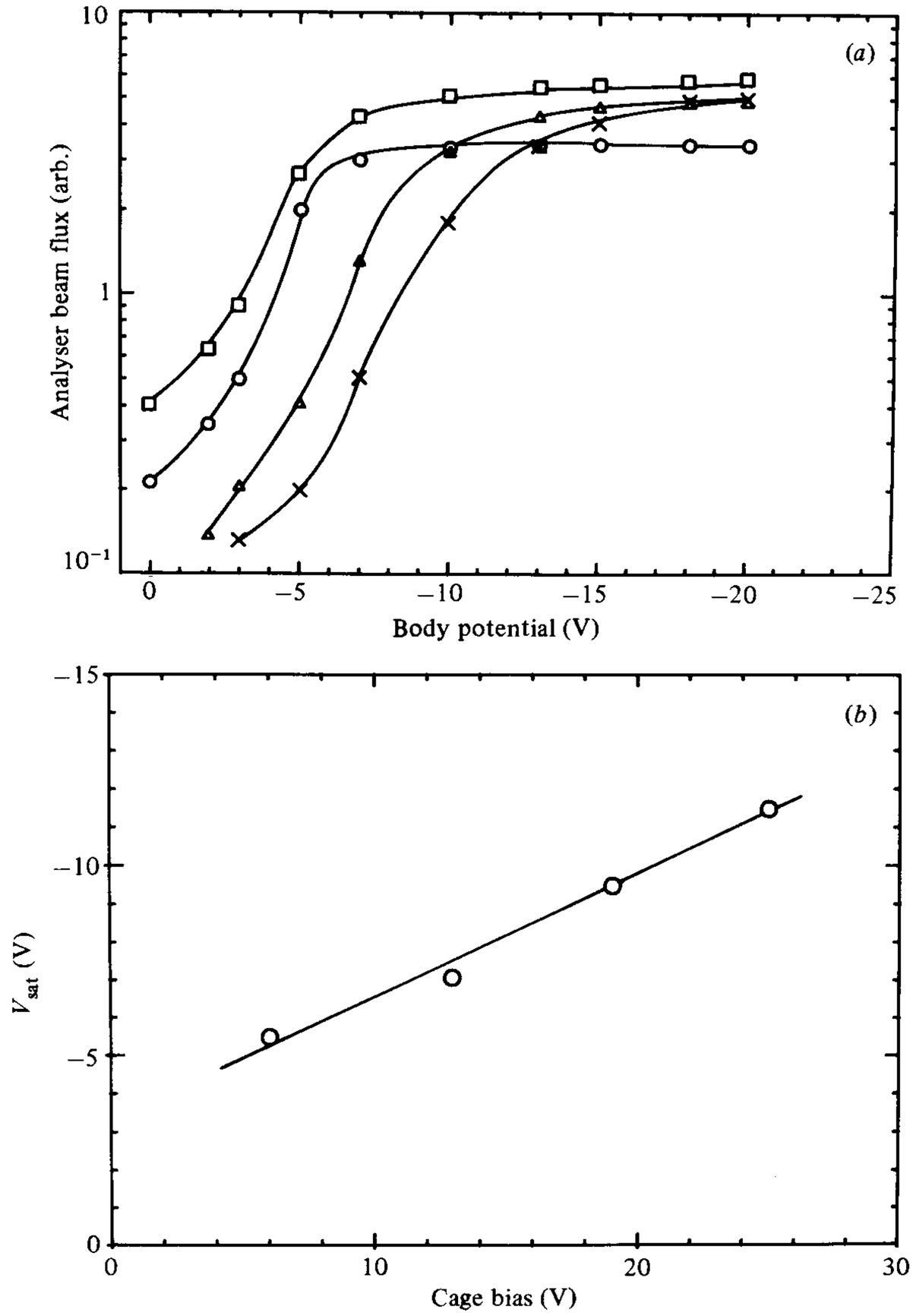


FIGURE 4. Summary of the effect of varying the body potential and cage voltage. (*a*) Analyser beam fluxes at 4·5 cm downstream of the obstacle *vs.* body potential showing a saturation effect which occurs at more negative values of $V_{body}$ for increasing values of $V_{cage}$: ○, 6 V; □, 13 V; △, 19 V; ×, 25 V. (*b*) Saturation voltage $V_{sat}$ *vs.* cage bias.

target was set at $\approx -20$ V, so that the body floated at a potential of $\approx -21$ V. The thermal background flux, which is about the same for the floating and grounded case, is also shown. The plasma potential in the target, for these conditions, is a few volts negative. Notable in this figure is the large ion density depression behind the grounded disk and the large ion density enhancement, on axis, behind the floating disk (disk edge positions indicated by vertical arrows). At the magnetic field present in this case ($\approx 8$ G), the gyroradius of the ions is relatively large (tens of cm for the thermal ions) while the ($\approx 1$–4 eV) electrons have gyroradius, $\rho_e \approx 0{\cdot}3$–$0{\cdot}6$ cm. The ion beam flux (at a fixed distance, 4·5 cm, behind the body) is shown in figure 3(*a*) for several values of

the body potential. The data in figure 3 were taken under conditions identical to those of figure 2; however, in this case, the beam flux profiles were taken with a fixed voltage (+9 V) on the retarding grid. The transition from an ion 'void' to an ion 'enhancement' occurs at a disk potential between 0 V and −4 V, i.e. when the disk begins being negative relative to the plasma space potential. Figure 3(*b*) shows profiles of beam flux, at a fixed body potential, for several values of the cage bias (ion beam energy). For low values of the cage bias, the ions are easily deflected to the wake axis in the vicinity of the analyser. As the cage bias is increased, the ion beam flux on axis at the analyser position begins decreasing, and by $V_{\text{cage}} = 40$ V the ion flux peak is no longer present since, presumably, the point at which the ion streams converge to form a significant flux peak now occurs further downstream of the analyser. Measurements similar to those shown in figure 3 were taken at various other values of the cage bias (i.e. ion beam energy) and body potential. These results are shown in figure 4(*a*) where the ion beam flux, on axis, is plotted against the body potential. The data in figure 4(*a*) indicate that the beam flux at a fixed distance behind the body increases with the (negative) body potential up to a point and then levels off. For higher cage bias (higher beam energy) higher negative voltage on the body is required to deflect the beam onto the wake axis. The saturation point ($V_{\text{sat}}$) on these curves (i.e. the body voltage at which the beam flux begins to level off) is interpreted as the minimum potential needed to deflect the ions to the analyser position. A plot of this saturation voltage *vs.* cage voltage (beam energy) is shown in figure 4(*b*). The data seem consistent with a linear relationship. We have also studied the effect which increasing the magnetic field has on the ion peak. As the magnetic field is increased, the height of the peak is reduced and the peak is broadened when the ion gyroradius (for a perpendicular ion energy of ≈0·1–0·2 eV) is of the order of the transverse body size.

The data presented in figures 2–4 suggests that the ions are deflected onto the wake axis as they pass near the edge of the body. That, indeed, the electric field near the edge of the body is important for ion deflection can be seen in the following set of data taken with the segmented body described in §2. The full 3 cm disk was replaced by a disk (2·2 cm diameter) and ring (3 cm OD; 2·4 cm ID) combination, separated by a thin ceramic insulator (see the insert in figure 5(*a*)). Analyser (A1) flux measurements (beam ions and thermal background) taken with various combinations of ring and disk potentials are shown in figure 5. For the particular conditions of figure 5 ($V_{\text{cage}} = 13$ V, $p = 5 \times 10^{-5}$ torr, $B = 23$ G), the space potential in the target was close to 0 V. We see then, in figure 5(*a*), a large depression in the ion beam flux on axis when both the ring and disk are biased at 0 V. If the disk is biased to −15 V and the ring left at 0 V, there is still a large depression in the beam flux behind the body as shown in figure 5(*b*). When, however, the ring is biased negatively relative to the plasma space potential, the axial ion peak is observed, whether or not the disk is also biased negatively. Comparing figure 5(*c*) and 5(*d*) we see clearly that the ring must be biased negatively in order to produce the ion peak on axis.

Measurements of the axial dependence of the ion beam flux behind the body were made using analyser A2 which could be moved axially and rotated about the vertical through the wake. These measurements were taken at $p \approx 5 \times 10^{-5}$ torr, $B \approx 1{\cdot}5$ G, and for various values of the cage bias (ion beam

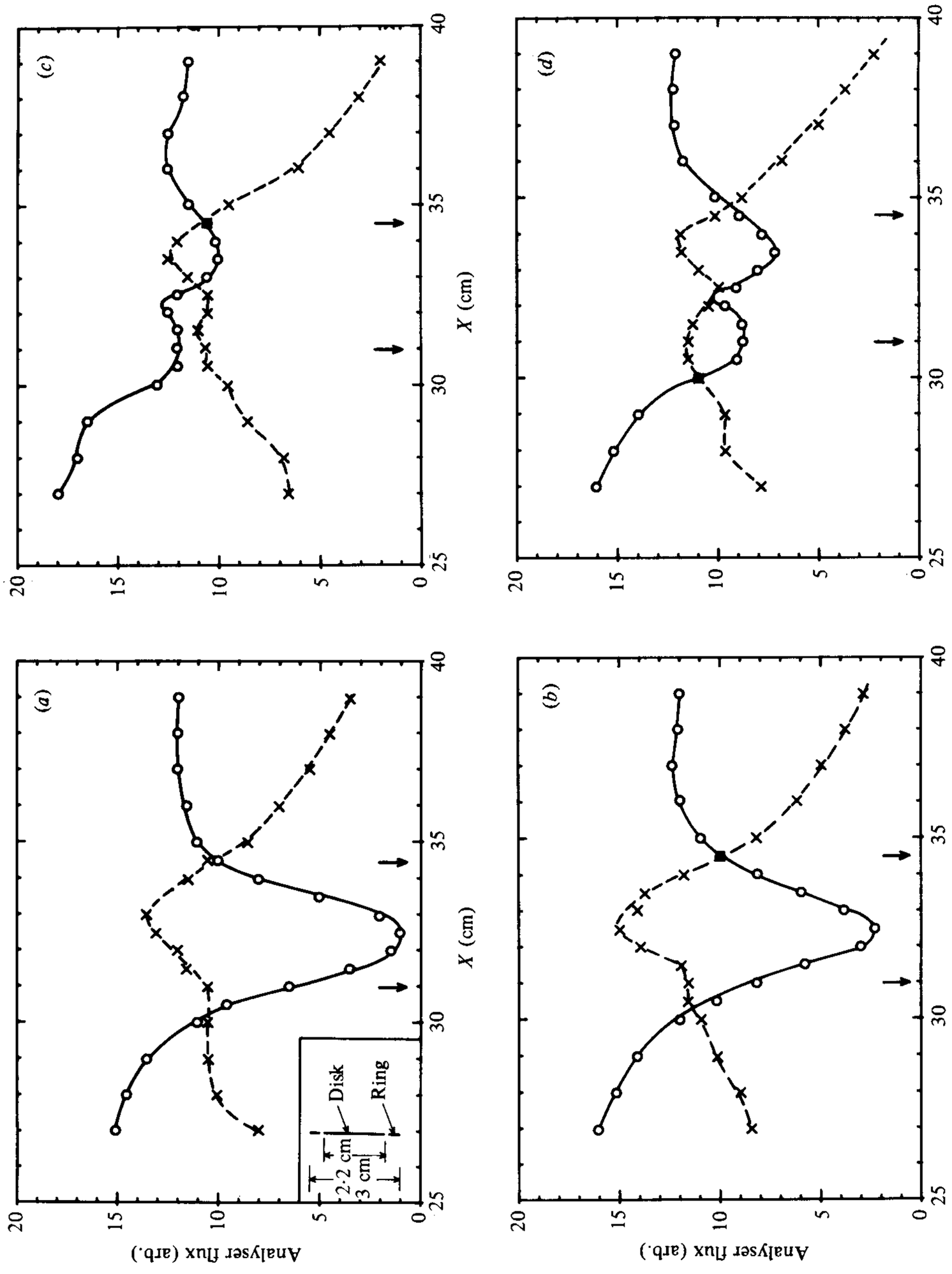


FIGURE 5. Analyser beam flux (○) and thermal flux (×) measurements taken with the ring+disk combination, for various combinations of ring bias ($V_{ring}$) and disk bias ($V_{disk}$) (*a*) $V_{ring} = 0$ V, $V_{disk} = -15$ V; (*b*) $V_{ring} = 0$ V, $V_{disk} = 0$ V; (*c*) $V_{ring} = -15$ V, $V_{disk} = 0$ V; (*d*) $V_{ring} = -15$ V, $V_{disk} = 0$ V. Insert in (*a*) shows ring+disk schematic.

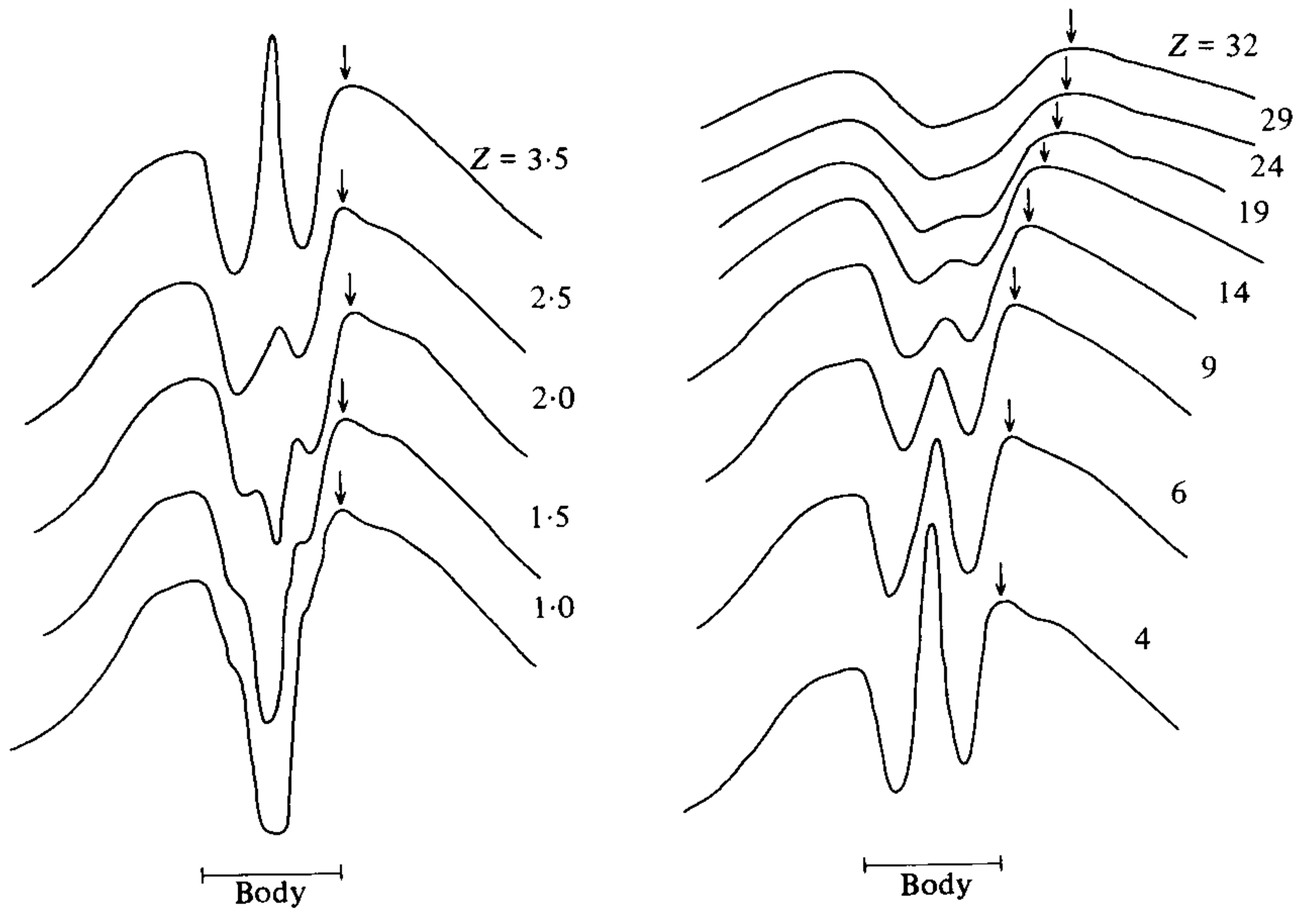


FIGURE 6. Radial profiles of the analyser beam flux at various axial positions downstream of the body. The values of $Z$ refer to distances in cm behind the body. The arrows mark the location of the right edge of the wake.

energy) and body potential. Figure 6 shows a series of radial profiles of ion beam flux (at a fixed retarding grid voltage) at various axial positions behind the body, with $V_b = -5$ V, and $V_{\text{cage}} = +36$ V. The number labelling each plot is the distance in centimetres behind the body, with the furthest downstream position corresponding to $\approx 10$ body diameters ($Z/R \approx 20$). Referring to figure 6, we see at $Z = 1$ cm and $Z = 1{\cdot}5$ cm the appearance of 'shoulders' in the flux profiles which propagate inward (toward the axis) as $Z$ increases. Two well defined peaks, on either side of the wake axis, are observed at $Z = 2{\cdot}0$ cm. By $Z = 2{\cdot}5$ cm the features merge into the axial ion peak, which continues to increase in amplitude, reaching its maximum (for these particular conditions) by about $Z = 4$ cm. Proceeding further downstream of the body, the peak gradually diminishes in amplitude until it finally disappears by $Z = 29$ cm. Also evident in the data of figure 6 is the broadening of the density depletion in the wake as one moves in the downstream direction. This is observed as the apparent propagation of the wake edge into the background plasma. A number of measurements, similar to those shown in figure 6, were made at the same cage bias (36 V) but at body potentials of $-18$ V, 0 V, $+5$ V, and $+9{\cdot}5$ V. For a cage bias of 36 V the plasma potential in the target was $+10{\cdot}5$ V, so that, for all values of $V_b$ used, the body was at a negative potential relative to the plasma. From these measurements we can construct the type of plot in figure 7 which shows the general two-dimensional structure of the wake. The lower part of figure 7 shows the trajectories of the ions deflected onto the wake axis. The angle of the trajectory depends critically on the body potential, with the axis convergence point, $Z_{\text{max}}$, occurring closer to the body as $V_b$ becomes more negative. This effect is summarized in the logarithmic plot in figure 8 of $Z_{\text{max}}$ *vs.* the deflection voltage, $V_{\text{def}} = |V_b - V_{\text{sp}}|$, $V_{\text{sp}}$ being the plasma space potential. The data show a reasonable agreement with a dependence $Z_{\text{max}} \propto V_{\text{def}}^m$, with $m \approx -0{\cdot}5$. The implications of this dependence will be discussed in §4.

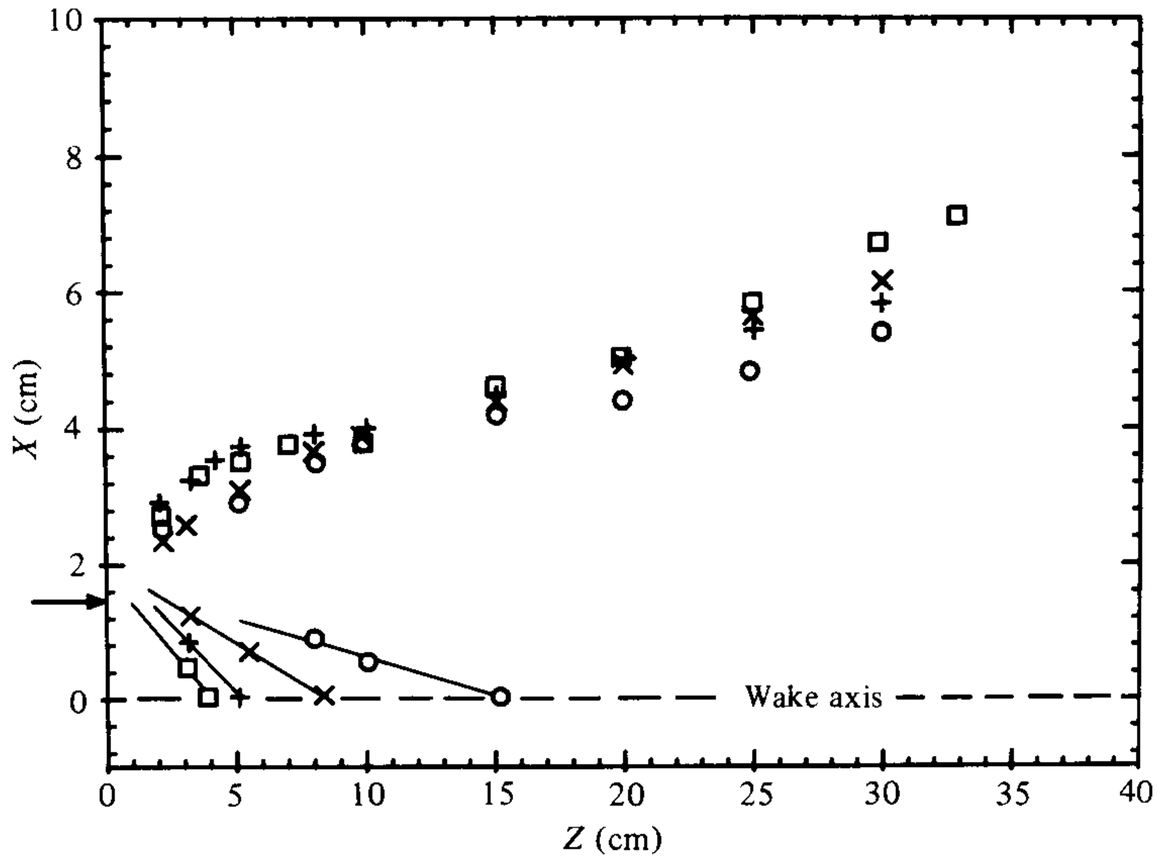


FIGURE 7. Two-dimensional structure of the wake showing the trajectory of the incoming ion streams deflected onto the wake axis (bottom) and the outgoing density rarefaction (top). $V_{cage} = 36$ V and values of $V_{body}$ are □, −5 V; +, 0 V; ×, 5 V; ○, 9·5 V.

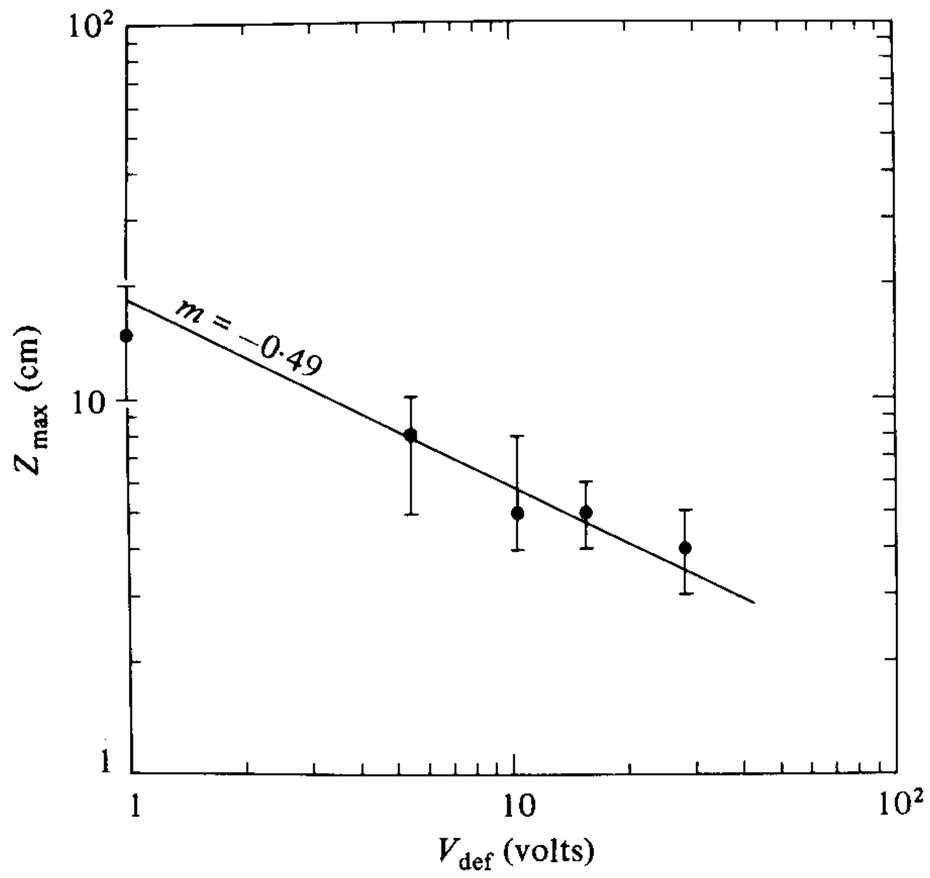


FIGURE 8. Log–log plot of the axial convergence point of the ion streams, $Z_{max}$, *vs.* the deflection voltage $V_{def} = |V_b - V_{sp}|$.

The cluster of points in the upper portion of figure 7 refers to the location of the wake edge, which exhibits an outward propagation as one moves in the downstream direction. Note that, in contrast to the converging ion streams, this diverging feature propagates outward at an angle to the wake axis which is nearly independent of the body potential. We interpret this effect as a density rarefaction (see, for example, Raychaudhuri *et al.* 1986) which, in the flowing plasma, propagates radially outward, at the ion acoustic speed. Quantitatively,

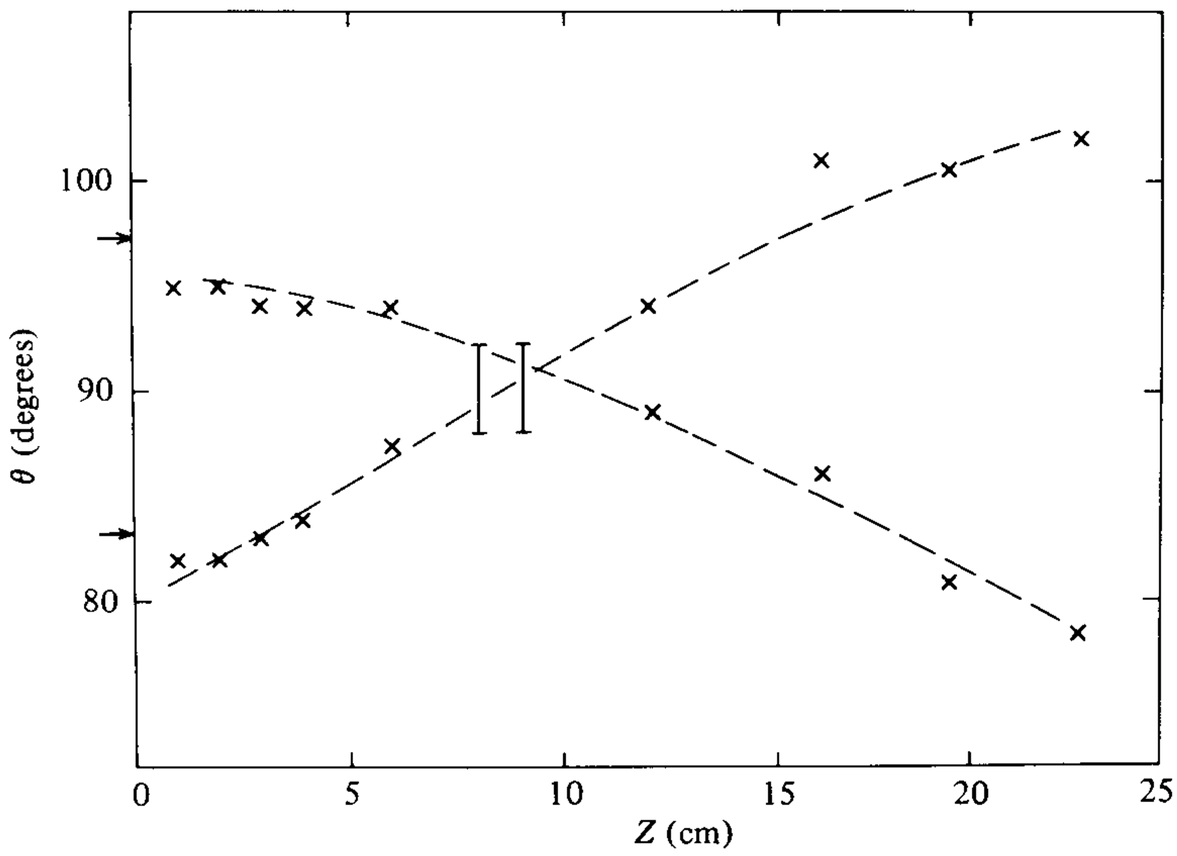


FIGURE 9. Locations of maximum noise amplitude in the wake region. $\theta$ is the angle between the analyser and the vertical as the analyser is rotated transvèrsely through the wake.

the propagation angle agrees roughly with the so-called Mach angle $\tan\theta_M = M^{-1}$, where $M$ is the Mach number of the flow.

### 3.2. *Plasma noise in the wake*

In this section we present some preliminary results on the nature and spatial distribution of plasma noise in the wake. The measurements were made with analyser A2, by monitoring the spectra (using an HP8557A spectrum analyser) of the fluctuations in the analyser collector current with a fixed voltage ($-9$ V) on the retarding grid. The locations of maximum noise amplitude at several axial positions were determined by rotating A2 through various angles ($\theta$) about the vertical. In general, the noise was broad-band (FWHM $\approx 50$ kHz) and peaked at about 40–50 kHz. The spatial mapping of the maximum noise amplitude is shown in figure 9. Immediately behind the body, the noise amplitude is largest at the wake edge, but the location of maximum amplitude moves closer to the wake axis as one moves in the downstream direction. At an axial location between $\approx$7–11 cm, the maximum noise amplitude occurs on the wake axis. For $Z \gtrsim 11$ cm, a noise minimum is again observed on axis, while noise maxima occur further and further (radially) from the axis as one moves downstream. In attempting to understand the noise structure in the wake, two additional observations need mentioning: (i) for the particular conditions of figure 9, the 'convergence point' of the noise peaks (7–11 cm) is actually further downstream of the crossing point of the ion beams, which occurs at about 4 cm, and (ii) the same general level and spectral shape of noise is present in regions other than the wake; for example, it is also present in front of the object.

## 4. Discussion

We have presented data from a laboratory experiment relevant to the problem of the disturbance produced by a stationary body in a supersonic (ion)

flow. This investigation has been mainly concerned with the situation in which the conducting body is at a negative potential relative to the ambient plasma potential, which is usually the case for electrically floating objects. In particular, our results show that the formation of the axial ion peak due to the electrostatic deflection of ions onto the wake axis is closely connected with a radially inward electric field appearing near the outer portion of the obstacle (cf. figure 5). The importance of electric fields near the edge of an obstacle was also emphasized by Schmitt (1973) who showed that, with a thick obstacle, ions would be deflected into the side of the obstacle so that no axial ion peak was formed. Ion deflection has been observed by others and discussed theoretically, in particular by Taylor (1967) and Martin (1974). As Taylor (1967) points out, there are two different fields to consider in the wake: (*a*) the electric field associated with the body sheath, and (*b*) the electric field which may be set up by the negative space charge of electrons which tend to move into the wake faster than the ions. The combination of these two effects may result in a sheath surrounding the body that is elongated along the wake (see figure 2 of Taylor (1967)). In figure 10 we illustrate, schematically, the effect which an inwardly directed electric field has on ions passing close to the body. Figure 10(*a*) refers to the case in which the ions receive an impulsive, inward 'kick' by the electric field at the body edge. If, however, the sheath is elongated, as shown in figure 10(*b*), the ions are continuously deflected as they approach the wake axis.

With the simplest assumptions we can easily see that the two cases shown in figure 10 give rise to different dependences between body potential, $V_b$, the ion beam energy, $E_i$, and the axial position of the convergence point of the deflected ion beams, $Z_{\max}$. If we assume, for case 10(*a*), that the electric field is constant in the sheath and extends laterally over approximately 1 $\lambda_D$, and axially over approximately 2 $\lambda_D$ ($\lambda_D$ = Debye shielding distance), we find

$$Z_{\max} \propto RE_i/V_b, \tag{1}$$

where $R$ is the body radius. Martin (1974), on the other hand, assumes that a constant electric field, proportional to the body potential, is present in the elongated sheath (figure 10(*b*)) which extends into the wake and arrives at

$$Z_{\max} \propto (RE_i/V_b)^{\frac{1}{2}}. \tag{2}$$

Thus, the two situations of figure 10(*a* and *b*) give rise to somewhat different parameter dependences of $Z/R$.

Our data suggest (see figure 5) that the deflection of ions is primarily connected with a negative bias on the *outer* portion of the obstacle. This would seem to be in line with the picture of figure 10(*a*) in which the ions receive an impulsive kick at the obstacle edge and then follow a straight line trajectory to the wake axis. However, the parametric dependence of $Z_{\max}$ on $V_b$ (figure 8) is more consistent with the situation of figure 10(*b*), since we found that $Z_{\max} \propto V_b^{-\frac{1}{2}}$. At a given $Z_{\max}$, the data of figure 4 indicate a proportionality of $V_b$ and $E_i$, which is true, of course, for both 10(*a*) and 10(*b*).

We believe it may also be possible to explain the $V_b^{-\frac{1}{2}}$ dependence of $Z_{\max}$ by envisaging the situation shown in figure 10(*c*). In this picture we assume that the effect of the edge potential on the body is to produce an elongated sheath in the outer annular region of the wake. We assume, for simplicity, that a uniform, inward electric field, **E**, is present in this sheath and, further, that this

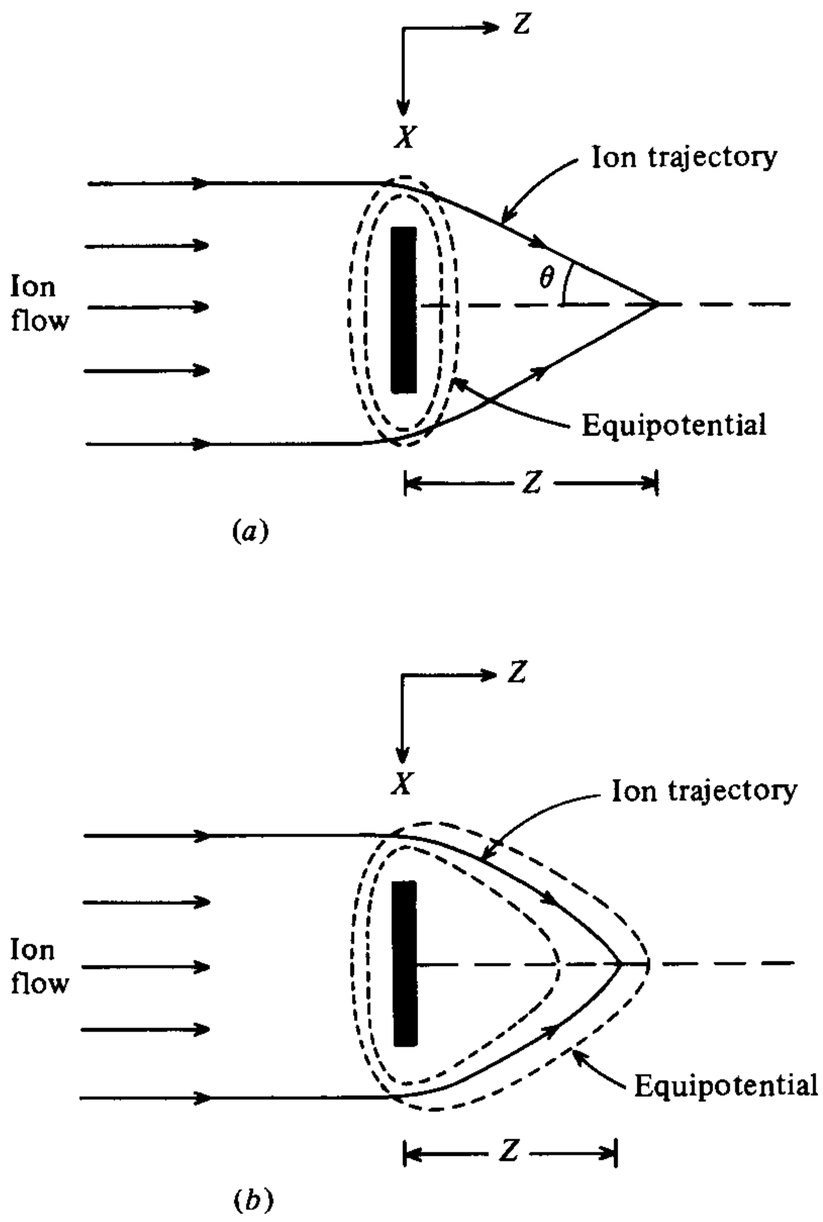


FIGURE 10. Schematic diagrams of the body sheath structure and deflected ion streams. (*a*) Impulsive deflection of ions in the body sheath. (*b*) Continuous deflection of ions in a body sheath extended to the wake axis. (*c*) Deflection of ions in a body sheath extended along the wake edge.

electric field is directly related to the body potential, i.e. $|\mathbf{E}| \propto V_b$. An ion of energy $E_i$ and impact parameter $b$ relative to the body edge will enter the sheath, be continuously deflected until it exits the sheath and then coast in a straight line path to the wake axis a distance $Z(b)$ behind the body. The analysis of this situation is straightforward and leads to the following expression for $Z(b)$:

$$Z(b) \propto (E_i/V_b)^{\frac{1}{2}}[2b^{\frac{1}{2}} + Rb^{-\frac{1}{2}}]. \tag{3}$$

This relation shows that, for ions with a given impact parameter, the location of the crossing point of the deflected ions scales as $(E_i/V_b)^{\frac{1}{2}}$, which is the same scaling as that obtained for the situation of figure 10(*b*). This simple picture may be useful as a first step in understanding how the electric field near the edge of the body deflects ions, and in explaining the observed parametric dependences of the axial convergence point. The model could be refined by including a spatially dependent electric field in the sheath.

The final observation to discuss is that of the plasma noise in the wake region. This noise occurs in the frequency range near $\approx 50$ kHz which is below the ion plasma frequency, $f_{pi} \simeq 0{\cdot}3$–1 MHz, estimated from either the flowing plasma or the background plasma density. Although we cannot offer any quantitative explanation for the spectral or spatial distribution of the noise, we can point out that a similar noise structure has been reported in the near wake of the space shuttle. Murphy *et al.* (1986) have observed density fluctuations, with $\Delta n/n$ equal to few per cent, which peak generally in the region of the steepest density gradients, i.e. in the transition zone between the ram and wake of the shuttle. Our data also show near-wake noise peaks near the wake edge, with a noise minimum on the wake axis. The distribution of noise does depend, however, on the downstream wake distance.

It is important also to emphasize that, while in our present experiments the plasma flow is magnetic field-aligned, the plasma flow around the space shuttle is, generally, at a finite angle to the earth's magnetic field. We intend to perform experiments, at some later time, in which the plasma flow will be at a finite angle to the applied magnetic field.

We wish to thank Al Scheller and Rick Ross for their technical assistance. This work was supported by the Strategic Defense Initiative Organization through the Office of Naval Research and by The Office of Naval Research.

## REFERENCES

D'Angelo, N. & Merlino, R. L. 1986 *IEEE Trans. on Plasma Science.* **PS-14**, 609.

Martin, A. R. 1974 *Planet. Space Sci.* **22**, 121.

Murphy, G., Pickett, J., D'Angelo, N. & Kurth, W. S. 1986 *Planet. Space Sci.* **34**, 993.

Nosachev, L. V. & Skvortsov, V. V. 1978 *Soviet Phys. Tech. Phys.* **23**, 658.

Raychaudhuri, S., Hill, J., Chang, H. Y., Tsikis, E. K. & Lonngren, K. E. 1986 *Phys. Fluids* **29**, 289.

Samir, U., Wright, K. H. & Stone, N. H. 1983 *Rev. Geophys. Space Phys.* **21**, 1631.

Schmitt, J. P. M. 1973 *Plasma Phys.* **15**, 667.

Stone, N. H. 1979 Ph.D. Thesis, University of Alabama in Huntsville.

Stone, N. H. 1981*a* *J. Plasma Phys.* **26**, 351.

Stone, N. H. 1981*b* *J. Plasma Phys.* **26**, 385.

Stone, N. H., Oran, W. A. & Samir, U. 1972 *Planet. Space Sci.* **20**, 1787.

Taylor, J. C. 1967 *Planet. Space Sci.* **15**, 155.

Wright, K. H., Stone, N. H. & Samir, U. 1985 *J. Plasma Phys.* **33**, 71.